Spin-orbit-proximitized ferromagnetic metal by monolayer transition metal dichalcogenide: Atlas of spectral functions, spin textures, and spin-orbit torques in Co/MoSe$_2$, Co/WSe$_2$, and Co/TaSe$_2$ heterostructures

Kapildeb Dolui and Branislav K. Nikolić[*]
Department of Physics and Astronomy, University of Delaware, Newark, Delaware 19716-2570, USA

The heterostructures composed of an ultrathin ferromagnetic metal (FM) and a material hosting strong spin-orbit (SO) coupling are the principal resource for SO torque and spin-to-charge conversion nonequilibrium effects in spintronics. The key quantity in theoretical description of these effects is *nonequilibrium spin density*, which can appear on any monolayer of the heterostructure through which the current is flowing as long as the monolayer bands are affected by the native or proximity induced SO coupling. Here we demonstrate how hybridization of wave functions of Co layer and a monolayer of transition metal dichalcogenides (TMDs)—such as semiconducting MoSe$_2$ and WSe$_2$ or metallic TaSe$_2$—can lead to *dramatic transmutation* of electronic and spin structure of Co within some distance away from its interface with TMD, when compared to the bulk of Co or its surface in contact with a vacuum. This is due to proximity induced SO splitting of Co bands encoded in the spectral functions and spin textures on its monolayers, which we obtain using noncollinear density functional theory (ncDFT) combined with equilibrium Green function (GF) calculations. In fact, SO splitting is present due to structural inversion asymmetry of the bilayer—i.e., just the presence of the interface—even if SO coupling within TMD monolayer is artificially switched off in ncDFT calculations. However, switching it on makes the effects associated with proximity SO coupling within Co layer about five times larger. Injecting spin-unpolarized charge current through SO-proximitized monolayers of Co generates nonequilibrium spin density over them, so that its cross product with the magnetization of Co determines SO torque. The SO torque computed via first-principles quantum transport methodology, which combines ncDFT with nonequilibrium GF calculations, can be used as the screening parameter to identify optimal combination of materials and their interfaces for applications in spintronics. In particular, we identify heterostructure two-monolayer-Co/monolayer-WSe$_2$ as *the most optimal* one, at least in the clean limit.

I. INTRODUCTION

The study of proximity effects, such as superconducting and magnetic, within bulk normal materials has a long history [1,2]. It has been rekindled with the advent of new materials and/or regimes of quantum coherence. For example, the mesoscopic regime of normal materials [3,4] at low temperatures hosts large-scale phase-coherent single electron states which can couple to macroscopically coherent many-body states on the superconducting side of the interface; both superconducting and magnetic proximity effects have been intensely explored [5] as soon as two-dimensional (2D) materials and their van der Waals heterostructures have been discovered. In the superconducting proximity effect [3,4,6–8], Cooper pairs leak from the superconductor to the normal material side, where the density of Cooper pairs decreases exponentially from superconductor/normal-material interface. Such creation of correlated electron-hole pairs and the corresponding change in the local properties of the normal material have been explored in metals [1,4], ferromagnets [9], 2D [10], and topological materials [11] brought into contact with

a superconductor. The *direct* effect is also accompanied by the *inverse* superconducting proximity effect [8,12] where the order parameter is depleted and electronic density of states is induced inside the superconducting energy gap within some length of the superconductor side of the interface.

The analogous *direct* magnetic proximity effect emerges when ferromagnetic metal (FM) induces nonzero local magnetization in the adjacent nonmagnetic material which decays exponentially away from the interface [2,13–16]. In FM/TMD heterostructures in the focus of this study, where FM is Co and TMD is monolayer (ML) of transition metal dichalcogenide (TMD), as illustrated in Fig. 1, the nonzero magnetic moment in the setup of Fig. 1(a) appears in Fig. 2 on the middle atomic plane of TMD monolayer. The layered structure of TMDs of the type MX$_2$ in Fig. 1—where M=Mo,W,Ta and X=Se—is formed by graphenelike hexagonal arrangement of M and X atoms bonded together to give X-M-X sandwich of three atomic planes. Within the sandwich, each M atom is covalently bonded to six X atoms, whereas each X atom is connected to three M atoms. For all TMDs considered in Fig. 2, the bands around the Fermi level are mainly due to d orbitals of the respective transition metal. Consequently, the Co layer induces an order of magnitude larger magnetic moment ($\sim$0.03 μ_B per metal atom) at the
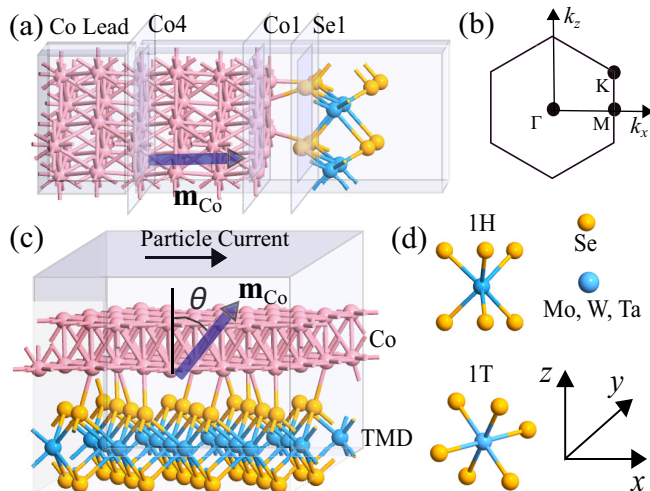
*bnikolic@udel.edu

FIG. 1. (a) Schematic view of heterostructures semi-infinite-Co(0001)/monolayer-TMD—where TMD = MoSe$_2$, WSe$_2$, or TaSe$_2$—which are employed in calculations of spectral functions [Eq. (10)] and the corresponding spin textures. These quantities are computed on planes passing through Se and Co atomic layer at the interface, denoted by Se1 and Co1, respectively, as well as on the 4th ML of Co away from the interface which is denoted by Co4. Panel (b) shows the in-plane hexagonal Brillouin zone of heterostructures in panel (a) with high-symmetry points marked—$\Gamma = (0, 0, 0)$, M = $(1/2, 0, 0)$ and K = $(1/3, 1/3, 0)$ in the units of reciprocal lattice vectors of the supercell—which define the high-symmetry k path employed in Fig. 3. (c) Lateral heterostructure 2ML-Co/monolayer-TMD, with unpolarized current injected parallel to its interface using small bias voltage V_b along the x axis in the linear-response regime. The heterostructure in (a) is assumed to be infinite (i.e., periodically repeated) in the yz plane, while the heterostructure in (c) is infinite in the xy plane. (d) Schematic view of 1H- and 1T-polytype structure of TMDs, in which transition metal atom has trigonal prismatic and octahedral coordination with Se atoms, respectively. 1T structure preserves the spatial inversion symmetry, whereas 1H structure does not.
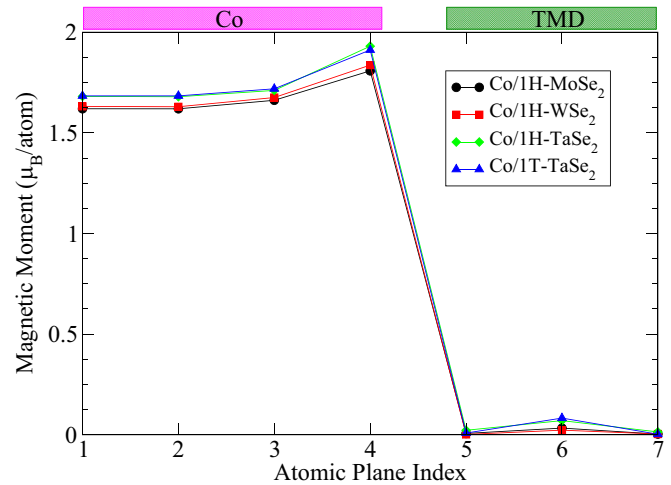

FIG. 2. Spatial profile of magnetic moments, averaged over all atoms within each atomic plane, for semi-infinite-Co/monolayer-TMD heterostructures illustrated in Fig. 1(a): (a) Co/1H-MoSe$_2$ (black circles); (b) Co/1H-WSe$_2$ (red squares); (c) Co/1H-TaSe$_2$ (green diamonds); and (d) Co/1T-TaSe$_2$ (blue triangles). Magenta and green solid boxes on the top of the panel show spatial extent of Co and TMD layers, respectively, as a guide to the eye.

transition metal atomic plane M, in comparison to that on the X=Se atomic planes.

In contrast to the inverse superconducting proximity effect, the inverse magnetic proximity effect can manifest either as enhancement or suppression of magnetic order on the FM side of the interface. For example, *enhanced* magnetic moments appear on the first ML of Co (denoted as atomic plane 4) in Fig. 2 which is in direct contact with monolayer TMD. Conversely, *reduced* magnetic moments in Co layer near the interface with heavy metals Pt or Ta are found in first-principles calculations in Fig. 4 of Ref. [17].

Recently the "proximity effect" terminology has been ported to describe how one material can be dramatically transformed by acquiring properties of its neighbor [5], even though the property acquired is not traditionally studied proximity superconductivity or magnetism. For example, normal metal [18,19], FM [20–22] or ferromagnetic insulator [23] in contact with metallic surface of three-dimensional topological insulator (TI) can acquire spin-momentum locking in their band structure, as one of the salient features of TI

materials [24], even though the Dirac cone energy-momentum dispersion on the TI side of the interface is typically heavily distorted by hybridization [20,22]. The long sought room-temperature noncollinear magnetic textures called skyrmions, with nontrivial topology in real space, have been achieved experimentally by moving away from bulk materials [25] to interfaces of ultrathin FM layers (composed of $\leqslant 3$ MLs) and heavy metals [26–28] which impart strong Dzyaloshinskii-Moriya interaction between magnetic moments on the FM side [29,30]. Once the inversion symmetry is broken due to the surface of FM or metals (such as Au, Ag, or Cu [31]) with vacuum, the Rashba type of spin-orbit (SO) coupling emerges in their Shockley surface state and it can penetrate over few MLs into the bulk [20]. Such interfacial SO coupling remains present around the interface, even if the surface is covered by normal metal without strong SO coupling effects, as exemplified by inversion asymmetric Cu/Co/Cu heterostructure [17] or by Co layer which remains SO proximitized (Fig. 6) despite SO coupling being artificially switched off on the TMD side of Co/TMD interface in Fig. 1(c).

As regards the traditional "proximity effect" terminology, which suggests fast decay of the proximity-acquired quantity away from the interface in analogy with superconducting and magnetic proximity effects, it is instructive to clarify different possibilities using examples of SO [32–35] or magnetic proximity effects [5,36–39] in (monolayer or multilayer) graphene and other 2D materials [38,40]. For example, when the evanescent wave function from semimetallic graphene penetrates into a ferromagnetic insulator (FI) where there are no states at the Fermi level, it acquires exchange splitting from the native ferromagnetism of the FI layer [39]. Conversely, the propagating wave function on the metallic surface of TI (or even normal metal like Cu [34]) or FM hybridizes with the wave function of graphene, thereby directly SO-splitting [33] or spin-polarizing [33,36,37] electronic structure of graphene,
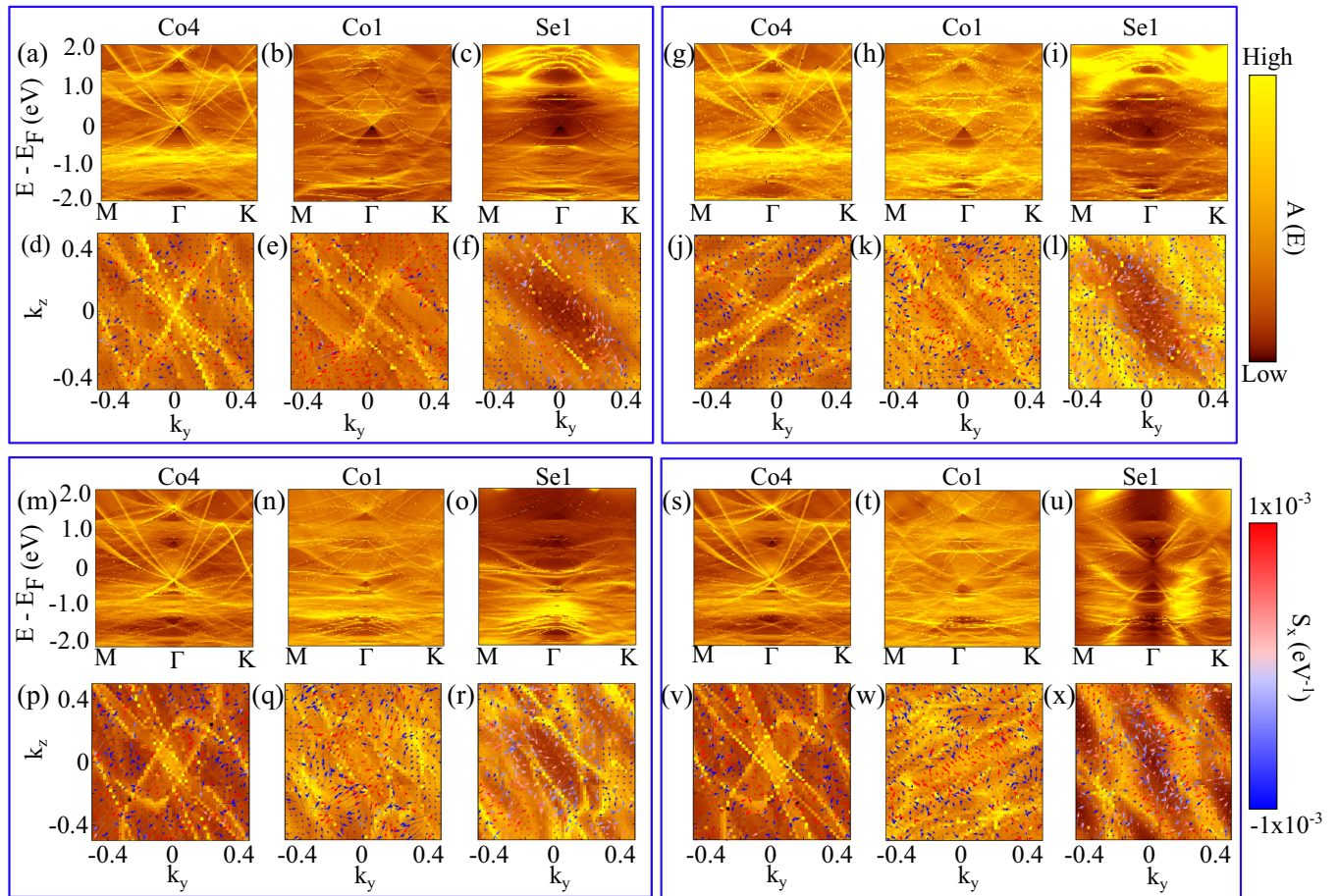
FIG. 3. Spectral function $A(E; k_y, k_z, x \in \{Co4, Co1, Se1\})$ plotted along the high-symmetry k path, M-Γ-K [Fig. 1(b)], at the atomic plane passing through (a) Co4, (b) Co1, and (c) Se1, as indicated in Fig. 1(a), of Co/1H-MoSe$_2$ heterostructure. The magnetization of semi-infinite Co layer is $\mathbf{m}_{Co} \parallel \hat{x}$ [Fig. 1(a)] and perpendicular to the interface. Panels (d)–(f) plot constant energy contours of $A(E - E_F = 0; k_y, k_z, x \in \{Co4, Co1, Se1\})$ at the Fermi energy $E - E_F = 0$ and the corresponding spin textures within the monolayers Co4, Co1, and Se1, respectively, where the out-of-plane S_x component of spin is indicated in color (red for positive and blue for negative values). Panels (g)–(l), (m)–(r), and (s)–(x) show the same information as panels (a)–(f) but for Co/1H-WSe$_2$, Co/1H-TaSe$_2$, and Co/1T-TaSe$_2$ heterostructure, respectively. The units for k_y and k_z are $2\pi/a$ and $2\pi/b$ where a and b are the lattice constants of the unit cell of the heterostructure.

respectively. The SO coupling can also be introduced by evanescent wave functions, as exemplified by metallic TaSe$_2$ in contact with insulating antiferromagnetic bilayer CrI$_3$ in which case SO proximity effect is exponentially decaying and it appears only on the first ML of CrI$_3$ in direct contact with TaSe$_2$ [40]. Such SO coupling "injected" by the proximity effect is also quite distinct from the native SO coupling of CrI$_3$ which is responsible for its magnetocrystalline anisotropy that stabilizes low-dimensional magnetism at finite temperature. Thus, when proximity effect is mediated by evanescent wave functions, it decays exponentially fast away from the interface akin to traditional superconducting and magnetic proximity effects. On the other hand, when it is mediated by hybridization of propagating wave functions, the acquired property can extend over long distances away from the interface (at least in clean systems). For heterostructures in Fig. 1(a), this is exemplified by the presence of proximity SO coupling-induced in-plane spin textures in Fig. 3 on the first ML Co1 directly at the interface, as well as on the fourth ML Co4 away from the interface. Thus, an ultrathin Co layer, such as 2 MLs of Co

in Fig. 1(b), or even up to 8 MLs employed in Fig. 7, will be fully SO proximitized over their whole volume. On the other hand, the SO proximity effect will slowly (but not exponentially) decay [20] into the bulk of semi-infinite layer in Fig. 1(a).

The SO-proximitized FM thin films have emerged as a major resource for spintronics, enabling effects like SO torque [41,42], spin-to-charge conversion [43], and skyrmion generation [29]. In the SO torque phenomenon, injecting unpolarized charge current parallel to the interface FM/SO-coupled-material induces current-driven (CD) nonequilibrium spin density $\mathbf{S}_{CD}$ which then drives the dynamics of the magnetization of FM layer via the SO torque $\propto \mathbf{S}_{CD} \times \mathbf{m}$ [41]. Here $\mathbf{m}$ is the unit vector along the magnetization direction of FM layer. Reciprocally, if nonequilibrium spin density is injected into the bilayer, such as by pumping of spin current due to precessing magnetization driven by microwaves [44–47], spin-to-charge conversion is initiated leading to charge current generation even in the absence of any bias voltage [48–50]. Although early theoretical studies of SO torque and
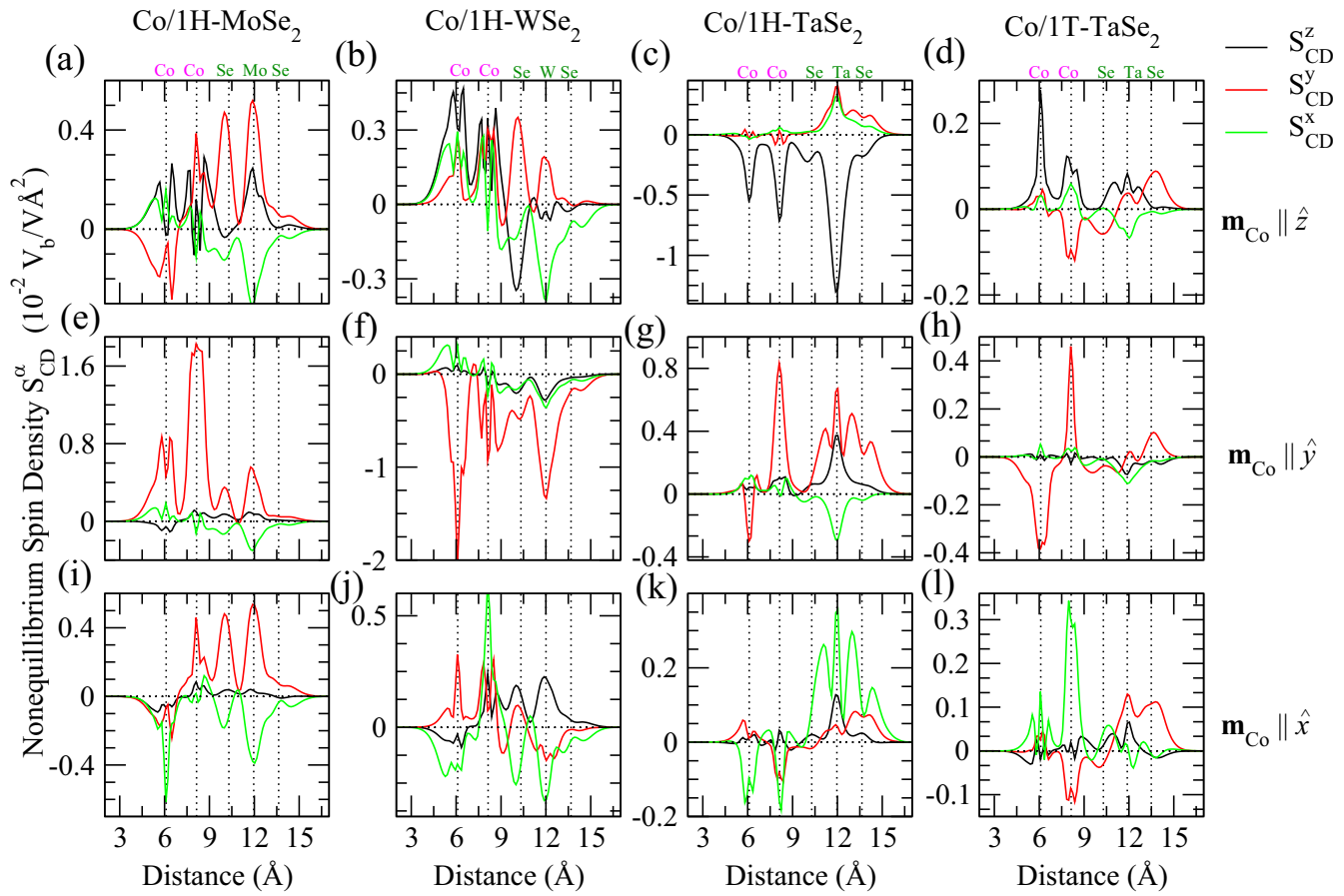
FIG. 4. The spatial profile of nonequilibrium spin density vector $\mathbf{S}_{CD}(z) = \mathbf{S}_{CD}^{even}(z) + \mathbf{S}_{CD}^{even}(z)$ [Eq. (9)] at the Fermi level for various 2ML-Co/monolayer-TMD heterostructures in Fig. 1(c) where monolayer TMD is: (a) 1H-MoSe$_2$; (b) 1H-WSe$_2$; (c) 1H-TaSe$_2$; and (d) 1T-TaSe$_2$. The magnetization of Co layer is perpendicular to the interface, $\mathbf{m}_{Co} \parallel \hat{z}$. Black, red, and green lines indicate z, y, and x components of $\mathbf{S}_{CD}(z)$, respectively. Panels (e)–(h) and (i)–(l) show the same information as panels (a)–(d) but for $\mathbf{m}_{Co} \parallel \hat{y}$ and $\mathbf{m}_{Co} \parallel \hat{x}$, respectively. Vertical dashed lines mark the position of each atom plane.

spin-to-charge conversion assume simplistic model Hamiltonians of the interface [50–53], it has been realized that three-dimensional (3D) geometry of transport is crucial to capture all relevant effects [49,54–56].

The simplistic tight-binding models of FM/SO-coupled-material bilayers defined on a 3D lattice can already capture some aspects of SO proximity effect [56], but first-principles calculations are required to accurately describe charge transfer, surface relaxation, and band bending between the two materials [19–22]. In this study, we delineate how properties of conventional room temperature FM, such as semi-infinite Co layer in the region near the interface in Fig. 1(a) or whole volume of ultrathin (of thickness ∼1 nm) Co layer in Fig. 1(c), can *dramatically* change due to just a single ML of adjacent TMD. Describing effects like complex spin textures (Fig. 3) within Co in equilibrium due to proximity SO coupling yields accurate first-principles Hamiltonian as an input for quantum transport calculations of CD nonequilibrium spin density $\mathbf{S}_{CD}$ (Figs. 4 and 5) on MLs of Co that host such textures. This also allows us to compute the corresponding SO torque $\propto \mathbf{S}_{CD} \times \mathbf{m}_{Co}$ (Figs. 5, 6, and 7).

Using these quantities as descriptors for screening public databases of band structures of 2D materials [57,58] and their heterostructures [59], or for screening "mini database" of

spectral functions and spin textures (Fig. 3) created in this study for a specific case of FM/TMD heterostructures, makes it possible to precisely identify combinations that maximize features of relevance for spintronics applications. For example, for Co/TMD heterostructure and three different TMDs investigated, we identify Co/1H-WSe$_2$ as the optimal combination for maximum SO torque, as demonstrated in Fig. 5. The complex angular dependence of SO torque in Co/1H-WSe$_2$ heterostructure is then investigated further in Fig. 6 where we demonstrate that even with SO coupling artificially switched off on the WSe$_2$ side, $\mathbf{S}_{CD}$ and thereby driven SO torque are nonzero due to overall broken inversion symmetry of the bilayer. Moreover, upon switching on the SO coupling in the first-principles calculations, SO torque is *enhanced* by about a factor of five in Fig. 6 and Table I, thereby further highlighting the value of computational screening of heterostructures by combined first-principles and quantum transport calculations.

The paper is organized as follows. In Sec. II we explain our first-principles quantum transport algorithm which combines nonequilibrium Green functions (NEGF) [60] with noncollinear density functional theory (ncDFT) calculations to directly compute SO torque components that are even or odd in the magnetization of FM layer. Section III A shows the results for spectral functions and spin textures in
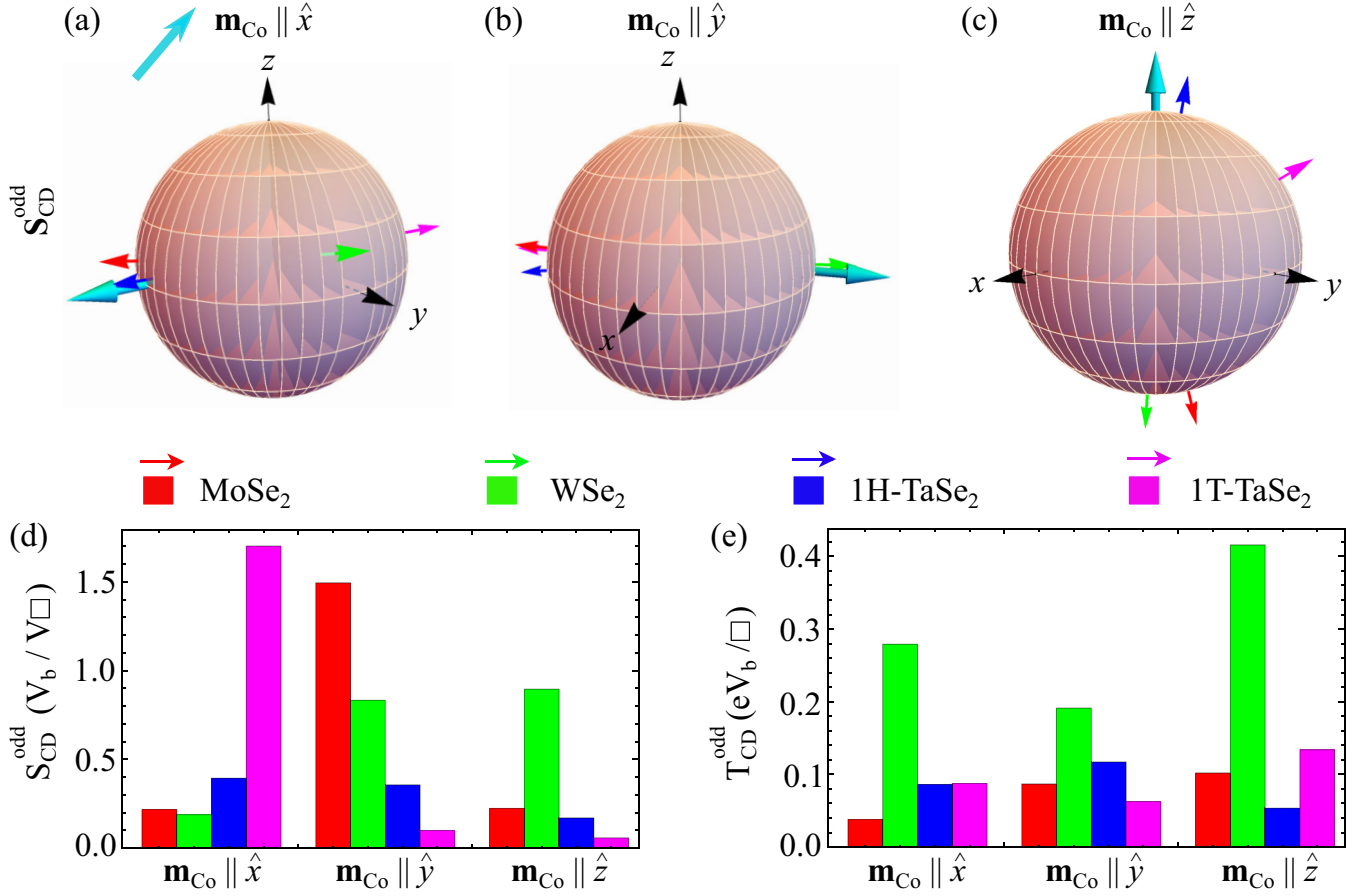
FIG. 5. (a)–(c) Direction of current-driven nonequilibrium spin density vector $\mathbf{S}_{CD}^{odd}$ [Eq. (9)] for magnetization $\mathbf{m}_{Co}$ (thick cyan arrow) in Fig. 1(c) oriented along the x, y, and z axis, respectively. Red, green, blue, and magenta arrows indicate the direction of $\mathbf{S}_{CD}^{odd}$ in Co/1H-MoSe$_2$, Co/1H-WSe$_2$, Co/1H-TaSe$_2$, and Co/1T-TaSe$_2$ heterostructures, respectively. Panels (d) and (e) are bar plots of the magnitudes $S_{CD}^{odd} = |\mathbf{S}_{CD}^{odd}|$ and $T_{CD}^{odd} = |\mathbf{T}_{CD}^{odd}|$, respectively, within 2 MLs of Co layer embedded into Co/1H-MoSe$_2$ (red bars), Co/1H-WSe$_2$ (green bars), Co/1H-TaSe$_2$ (blue bars), and Co/1T-TaSe$_2$ (magenta bars) heterostructures for different orientations of $\mathbf{m}_{Co}$. The area of the common rectangular supercell of these heterostructures is denoted by $\square = 4a \times 2\sqrt{3}a$, where a is the lattice constant of the respective TMD.

equilibrium on both sides of Co/TMD interface in Fig. 1(a). In Sec. III B, we discuss CD nonequilibrium spin density and thereby driven SO torque in Co/TMD lateral heterostructure depicted in Fig. 1(c) where unpolarized charge current is injected parallel to the interface. We conclude in Sec. IV.

II. MODELS AND METHODS

A. Spin-orbit torque from nonequilibrium density matrix expressed using NEGF

Both conventional spin-transfer torque, in spin valves or magnetic tunnel junctions containing two FM layers with noncollinear magnetizations [61–63], and SO torque [41], in setups such as the one in Fig. 1(c) containing *only one* FM layer, can be described microscopically and independently of particular physical mechanism [64–66] in a *unified* fashion as a consequence of local CD nonequilibrium spin density of conduction electrons $\mathbf{S}_{CD}(\mathbf{r})$ [16,63]. The cross product of this quantity with the local magnetization $\mathbf{M}(\mathbf{r})$ in the case of simplistic model Hamiltonians [52], or with the exchange-correlation (XC) magnetic field $\mathbf{B}_{XC}(\mathbf{r})$ of ncDFT [67,68] in the case of first-principles Hamiltonians [16,62–64,69], determines local spin torque $\mathbf{S}_{CD}(\mathbf{r}) \times \mathbf{B}_{XC}(\mathbf{r})$ at some point in space $\mathbf{r}$. Thus, the total torque is obtained by integrating over

TABLE I. Fitted coefficients (in the units of $eV_b/\square$) in the angular dependence [Eq. (13)] of the odd component of SO torque for 2ML-Co/monolayer-1H-WSe$_2$ heterostructure. The SO coupling of WSe$_2$ is either switched on ($\zeta_{WSe_2} \neq 0$) or off ($\zeta_{WSe_2} = 0$) in ncDFT calculations. The unit vector $\mathbf{p}$ in Eq. (13) is given in the second column for which $\mathbf{m}_{Co} || \mathbf{p}$ leads to $\mathbf{T}_{CD}^{odd} = 0$.

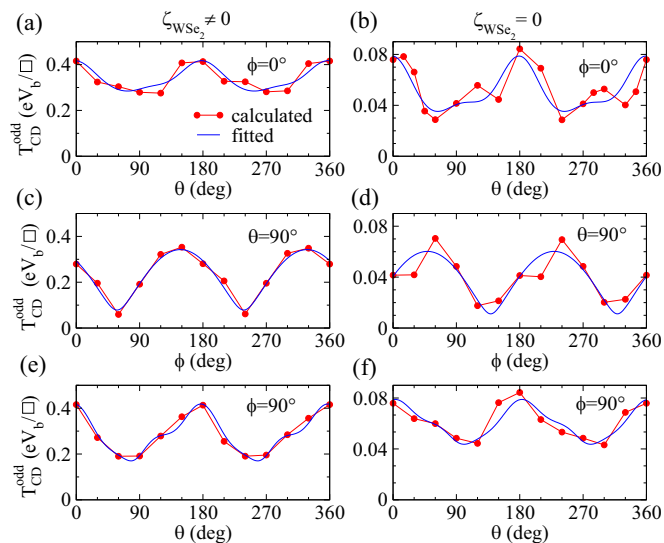|	$\mathbf{p} = (\theta, \phi)$	$T_{0\alpha}$	$T_{1\alpha}$	$T_{2\alpha}$	$T_{3\alpha}$	$T_{0\beta}$	$T_{1\beta}$
$\zeta_{WSe_2} \neq 0$	$(75°, 60°)$	0.416	-0.254	0.192	0.001	-0.092	0.105
$\zeta_{WSe_2} = 0$	$(105°, 120°)$	0.079	-0.038	0.063	-0.001	0.067	-0.014

FIG. 6. The azimuthal (θ) or polar (ϕ) angle dependence of the magnitude of the odd component of SO torque, $T_{CD}^{odd} \equiv |\mathbf{T}_{CD}^{odd}|$ [Eq. (8)], in 2ML-Co/monolayer-1H-WSe$_2$ heterostructure for: (a),(b) $\phi = 0°$; (c),(d) $\theta = 90°$; and (e),(f) $\phi = 90°$. In the left (right) column of panels $\mathbf{T}_{CD}^{odd}$ is computed with SO coupling in WSe$_2$ being turned on (off) in ncDFT calculations. Blue curves fit numerically computed red dots using expansion in Eq. (13), with nonzero fitting parameters listed in Table I.

FIG. 7. The layer-resolved magnitude of the odd component of SO torque $T_{CD}^{odd} \equiv |\mathbf{T}_{CD}^{odd}|$ in n-ML-Co/monolayer-1H-WSe$_2$ heterostructures where Co layer consists of 2 MLs—as in the illustration in Fig. 1 and as studied in Fig. 6—or 4, 6, and 8 MLs. The unpolarized charge current is injected parallel to the interface [i.e., along the x axis in Fig. 1(c)] and it flows through each of n MLs of Co layer. The total $\mathbf{T}_{CD}^{odd}$ on Co layer is the sum of contributions from each of these n MLs of Co.

the FM layer receiving the torque

$$\mathbf{T}_{CD} = \int_{FM} d^3r \, \mathbf{S}_{CD}(\mathbf{r}) \times \mathbf{B}_{XC}(\mathbf{r}). \tag{1}$$

Here $\mathbf{S}_{CD}(\mathbf{r}) = \text{Tr}\,[\rho_{CD}\check{\sigma}]$ is computed by tracing the CD contribution to the nonequilibrium density matrix [70]

$$\rho_{CD} = \rho_{neq} - \rho_{eq} \tag{2}$$

with the vector of the Pauli matrices $\check{\sigma} = (\sigma_x, \sigma_y, \sigma_z)$, where ρ_{eq} is the grand canonical density matrix of electrons in equilibrium [60,70]. The lesser Green function (GF)

$$\mathbf{G}^<(E) = i\mathbf{G}(E)[f_L(E)\mathbf{\Gamma}_L(E) + f_R(E)\mathbf{\Gamma}_R(E)]\mathbf{G}^\dagger(E) \tag{3}$$

of NEGF formalism [60] offers an efficient route to compute the nonequilibrium density matrix in the steady-state and elastic transport regime

$$\rho_{neq} = \frac{1}{2\pi i} \int_{-\infty}^{\infty} dE \, \mathbf{G}^<(E), \tag{4}$$

for arbitrary periodic or nonperiodic device setup by splitting it into two semi-infinite leads and the active region of the standard Landauer setup [60] for quantum transport calculations. In the case of SO torque, one typically [16,64–66,69] considers periodic setup in the xy plane, as exemplified by Co/TMD heterostructures in Fig. 1(c) whose semi-infinite leads and active region (of conveniently chosen length) are made of identical atoms. Here

$$\mathbf{G} = [E\mathbf{\Lambda} - \mathbf{H} - \mathbf{\Sigma}_L(E, V_L) - \mathbf{\Sigma}_R(E, V_R)]^{-1} \tag{5}$$

is the retarded GF; $\mathbf{H}$ is the matrix representation of (model of first-principles) Hamiltonian of the active region in some basis of localized orbitals basis $|\phi_i\rangle$; $f_{L,R}(E) = f(E - eV_{L,R})$
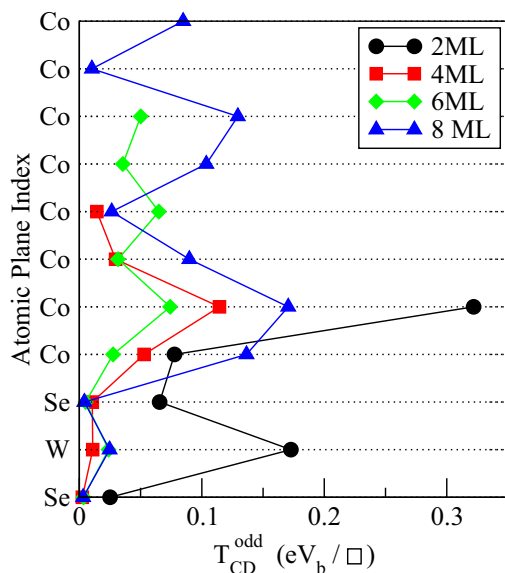
are the shifted Fermi functions of the left (L) and right (R) macroscopic reservoirs into which semi-infinite leads terminate; $V_b = V_L - V_R$ is the applied bias voltage between them; $\mathbf{\Sigma}_{L,R}(E, V_{L,R})$ are the self-energies of semi-infinite leads whose band bottom is shifted by the applied voltages; and $\mathbf{\Gamma}_{L,R}(E) = i[\mathbf{\Sigma}_{L,R}(E) - \mathbf{\Sigma}_{L,R}^\dagger(E)]$ are the level broadening matrices. Due to nonorthogonality of the basis of localized orbitals $|\phi_i\rangle$, we also use the overlap matrix $\mathbf{\Lambda}$ composed of elements $\langle\phi_i|\phi_j\rangle$. For lateral heterostructure in Fig. 1(c), all matrices depend on k_y, while for vertical heterostructure in Fig. 1(a) they depend on (k_x, k_y).

The spin-transfer torque is standardly split into two components [61–63], $\mathbf{T}_{CD} = \mathbf{T}_{CD}^{FL} + \mathbf{T}_{CD}^{DL}$. The fieldlike (FL) component is even under time reversal and it affects magnetization precession around the effective magnetic field. The dampinglike (DL) component is odd [71] under time reversal and it either enhances the Gilbert damping by pushing magnetization toward the effective magnetic field or it competes with the Gilbert term as "antidamping." Due to its more complex angular dependence [72], SO torque should be split into components which are odd or even in the magnetization of a single FM layer like $\mathbf{m}_{Co}$ in Fig. 1

$$\mathbf{T}_{CD} = \mathbf{T}_{CD}^{odd} + \mathbf{T}_{CD}^{even}. \tag{6}$$

Thus, it is also advantageous to decompose $\rho_{CD} = \rho_{CD}^{odd} + \rho_{CD}^{even}$ into the contributions whose trace with the Pauli matrices can yield directly $\mathbf{T}_{CD}^{odd}$ and $\mathbf{T}_{CD}^{even}$, respectively. This is achieved

by using the following expressions [63,73]

$$\boldsymbol{\rho}_{\text{CD}}^{\text{odd}} = \frac{1}{8\pi} \int_{-\infty}^{+\infty} dE [f_{\text{L}}(E) - f_{\text{R}}(E)](\mathbf{G}\boldsymbol{\Gamma}_{\text{L}}\mathbf{G}^{\dagger} - \mathbf{G}^{\dagger}\boldsymbol{\Gamma}_{\text{L}}\mathbf{G} - \mathbf{G}\boldsymbol{\Gamma}_{\text{R}}\mathbf{G}^{\dagger} + \mathbf{G}^{\dagger}\boldsymbol{\Gamma}_{\text{R}}\mathbf{G}), \tag{7a}$$

$$\boldsymbol{\rho}_{\text{CD}}^{\text{even}} = \frac{1}{8\pi} \int_{-\infty}^{+\infty} dE [f_{\text{L}}(E) - f_{\text{R}}(E)](\mathbf{G}\boldsymbol{\Gamma}_{\text{L}}\mathbf{G}^{\dagger} + \mathbf{G}^{\dagger}\boldsymbol{\Gamma}_{\text{L}}\mathbf{G} - \mathbf{G}\boldsymbol{\Gamma}_{\text{R}}\mathbf{G}^{\dagger} - \mathbf{G}^{\dagger}\boldsymbol{\Gamma}_{\text{R}}\mathbf{G}) - \frac{1}{2\pi} \int_{-\infty}^{+\infty} dE [f_{\text{L}}(E) + f_{\text{R}}(E)]\text{Im}\,\mathbf{G}$$

$$+ \frac{1}{\pi} \int_{-\infty}^{\infty} dE\,\text{Im}\,\mathbf{G}_0(E)f(E). \tag{7b}$$

Here $\mathbf{G}_0(E)$ is retarded GF in equilibrium obtained from Eq. (5) by setting $V_{\text{L}} = V_{\text{R}} = 0$, and the last term in Eq. (7b) is $-\boldsymbol{\rho}_{\text{eq}}$ [60,70]. In the limit of small bias voltage when compared to the Fermi energy E_F, $eV_b \ll E_F$, we can replace $[f_{\text{L}}(E) - f_{\text{R}}(E)] \mapsto -eV_b \partial f/\partial E$. Then, in the spirit of the linear-response theory, one can use $\mathbf{G}(E) \mapsto \mathbf{G}_0(E)$ with no bias voltage and thereby induced voltage drop across the active region in the Fermi surface terms in Eq. (7) which multiply $[f_{\text{L}}(E) - f_{\text{R}}(E)]$. However, in the second term in Eq. (7b) multiplying $[f_{\text{L}}(E) + f_{\text{R}}(E)]$ one needs to use the voltage drop [16,70]. This also requires us to assume the presence of some type of disorder since voltage drop is not allowed in ballistic systems. To reduce the computational expense, one can assume linear potential drop and use equilibrium charge and spin densities for all atoms as inputs in the Kohn-Sham Hamiltonian [Eq. (11)], instead of performing fully self-consistent calculations for the whole system [16].

Instead of real space calculations utilizing Eq. (1), for computational convenience we perform trace in the basis of localized pseudoatomic orbitals [74]

$$\mathbf{T}^{\text{even,odd}} = \frac{1}{\Omega_{\text{BZ}}} \int_{\text{BZ}} dk_y \,\text{Tr}\big[\boldsymbol{\rho}_{\text{CD}}^{\text{even,odd}}(k_y)\check{\boldsymbol{\sigma}} \times \boldsymbol{\Lambda}^{-1}\check{\mathbf{B}}_{\text{XC}}(k_y)\big]. \tag{8}$$

Here $\check{\mathbf{B}}_{\text{XC}}$ denotes a triple of matrices defined in Eq. (12). An additional integration over the one-dimensional Brillouin zone (BZ) of length Ω_{BZ} is performed because of assumed translational invariance of heterostructure in Fig. 1(c). The spatial profiles of $\mathbf{S}_{\text{CD}}(z) = \mathbf{S}_{\text{CD}}^{\text{even}}(z) + \mathbf{S}_{\text{CD}}^{\text{odd}}(z)$ in Fig. 4 are obtained from

$$\mathbf{S}_{\text{CD}}^{\text{even,odd}}(z) = \frac{1}{\Omega_{\text{BZ}}} \int_{\text{BZ}} dk_y \int dx\,\text{Tr}_{\text{spin}}\big[\boldsymbol{\rho}_{\text{CD}}^{\text{even,odd}}(x, k_y, z)\check{\boldsymbol{\sigma}}\big], \tag{9}$$

using $\boldsymbol{\rho}_{\text{CD}}^{\text{even,odd}}(x, k_y, z)$ in mixed real and k-space representation. Note that in Eq. (9) the superscript of $\mathbf{S}_{\text{CD}}^{\text{even,odd}}(z)$ follows the component $\boldsymbol{\rho}_{\text{CD}}^{\text{even,odd}}(x, k_y, z)$ used in the trace, rather than denoting behavior of nonequilibrium spin density under time reversal. Since the heterostructure in Fig. 1(c) is translationally invariant along the x axis, $\mathbf{S}_{\text{CD}}^{\text{even,odd}}(x, z)$ is a periodic function of x that is averaged in this direction over the supercell via Eq. (9) to obtain $\mathbf{S}_{\text{CD}}^{\text{even,odd}}(z)$ which depends on one spatial coordinate along the direction perpendicular to the interface [Fig. 1(c)].

B. Spectral functions and spin textures from equilibrium retarded GF

The spectral function (or local density of states) at an arbitrary plane at position x within the active region in Fig. 1(a) attached to only the left semi-infinite lead is extracted from the retarded GF in equilibrium $\mathbf{G}_0(E)$ using

$$A(E; \mathbf{k}_{\parallel}, x) = -\frac{1}{\pi}\text{Im}[\mathbf{G}_0(E; \mathbf{k}_{\parallel}; x, x)], \tag{10}$$

where $\mathbf{k}_{\parallel} = (k_y, k_z)$ for the coordinate system in Fig. 1. The diagonal matrix elements of $\mathbf{G}_0(E; \mathbf{k}_{\parallel}; x, x)$ are obtained from Eq. (5), where $\boldsymbol{\Sigma}_{\text{L}}(E) \neq 0$ and $\boldsymbol{\Sigma}_{\text{R}}(E) = 0$, by transforming it from orbital to real-space representation. At the chosen energy E and thereby defined constant energy contours, we compute the spin textures from the spin-resolved spectral function. We note that computed spectral functions and spin textures are exactly the same quantities measured on surfaces by spin-angle-resolved photoemission spectroscopy (spin-ARPES) [18,31]. However, spin-ARPES experiments cannot probe spectral functions and spin textures on buried planes that are too far below the surface because the penetration depth of low-energy photons is 2–4 nm.

C. Noncollinear density functional theory Hamiltonian of FM/TMD heterostructures

The ncDFT [67,68] operates with single-particle and spin-dependent Kohn-Sham (KS) Hamiltonian, which for the heterostructures in Fig. 1 is given by

$$\hat{H}_{\text{KS}} = -\hbar^2\nabla^2/2m + \hat{V}_{\text{H}}(\mathbf{r}) + \hat{V}_{\text{ext}}(\mathbf{r}) + \hat{V}_{\text{XC}}(\mathbf{r})$$
$$+ \hat{V}_{\text{SO}}(\mathbf{r}) - \boldsymbol{\sigma} \cdot \mathbf{B}_{\text{XC}}(\mathbf{r}). \tag{11}$$

Here $\hat{V}_{\text{H}}(\mathbf{r})$, $\hat{V}_{\text{ext}}(\mathbf{r})$, and $\hat{V}_{\text{XC}}(\mathbf{r}) = \delta E_{\text{XC}}[n(\mathbf{r}), \mathbf{m}(\mathbf{r})]/\delta n(\mathbf{r})$ are the Hartree, external, and the XC potentials, respectively; $\hat{V}_{\text{SO}}$ is additional potential due to SO coupling, and the XC magnetic field, $\mathbf{B}_{\text{XC}}(\mathbf{r}) = \delta E_{\text{XC}}[n(\mathbf{r}), \mathbf{m}(\mathbf{r})]/\delta \mathbf{m}(\mathbf{r})$, is functional derivative of spin-dependent XC energy functional $E_{\text{XC}}[n(\mathbf{r}), \mathbf{m}(\mathbf{r})]$ with respect to the vector magnetization density $\mathbf{m}(\mathbf{r})$. The extension of DFT to the case of spin-polarized systems is formally derived in terms of $\mathbf{m}(\mathbf{r})$ and total electron density $n(\mathbf{r})$. In the collinear DFT $\mathbf{m}(\mathbf{r})$ points in the same direction at all points in space, while in ncDFT $\mathbf{m}(\mathbf{r})$ can point in an arbitrary direction [67,68]. The matrix representation of the XC magnetic field, $\check{\mathbf{B}}_{\text{XC}}$, employed in Eq. (8), can be extracted from the matrix representation $\mathbf{H}_{\text{KS}}$ of $\hat{H}_{\text{KS}}$ using

$$\check{\mathbf{B}}_{\text{XC}} = (2\text{Re}[\mathscr{H}^{\uparrow\downarrow}], -2\text{Im}[\mathscr{H}^{\uparrow\downarrow}], \mathscr{H}^{\uparrow\uparrow} - \mathscr{H}^{\downarrow\downarrow}), \tag{12}$$

where $\mathscr{H} = \mathbf{H}_{\text{KS}} - \mathbf{V}_{\text{SO}}$. Note that in the presence of SO coupling, a term $\hat{V}_{\text{SO}}(\mathbf{r}) \propto \boldsymbol{\sigma} \cdot \check{\mathbf{L}}$, where $\check{\mathbf{L}}$ is the orbital angular momentum operator, is added in the KS Hamiltonian [Eq. (11)]. Thus, when the XC magnetic field is extracted from the KS Hamiltonian, $\hat{V}_{\text{SO}}(\mathbf{r})$ has to be subtracted as done in Eq. (12).

We employ the interface builder in QuantumATK [75] package to construct a unit cell for the bilayer heterostructure and use the experimental lattice constants. In order to determine the interlayer distance, we use Perdew-Burke-Ernzerhof (PBE) parametrization [76] of the generalized gradient approximation (GGA) for the XC functional as implemented in QuantumATK package [75]. We find the average interlayer distance between Co and TMDs in Fig. 1 in the range of 2.11–2.18 Å. The hexagonal supercell of Co(0001) and TMD(0001) surface is constructed using their hexagonal primitive lattice vectors $\{\mathbf{a}, \mathbf{b}\}$, where the lattice vectors of the supercell are $\{\mathbf{a} + 3\mathbf{b}, 2\mathbf{a} - \mathbf{b}\}$ and $\{2\mathbf{a}, 2\mathbf{b}\}$ for Co and TMDs surfaces, respectively. The lattice mismatches in Co/TMDs bilayers are 0.58%, 0.53%, 2.2%, and 2.4% for TMD = MoSe$_2$, WSe$_2$, 1H-TaSe$_2$, and 1T-TaSe$_2$, respectively. Subsequently, a rectangular geometry setup [Fig. 1(c)] is constructed from the common hexagonal supercell in order to calculate nonequilibrium spin density and SO torque.

The matrix representation $\mathbf{H}_{\text{KS}}$ employed in Eq. (5), $\mathbf{H} \mapsto \mathbf{H}_{\text{KS}}$, for the active region and self-energies $\boldsymbol{\Sigma}_{\text{L,R}}(E)$ of semi-infinite leads for heterostructures in Fig. 1 were computed using QuantumATK where we employ PBE parametrization of GGA; norm-conserving fully relativistic pseudopotentials of the type SG15-SO [74] for describing electron-core interactions; and SG15 (medium) basis of localized pseudoatomic orbitals [74]. Periodic boundary conditions are employed in the plane perpendicular to the transport direction [along the x axis in Fig. 1(c)], with a 1×6 k-point grid for self-consistent calculation. Nonequilibrium spin density and SO torque are then obtained by integrating over a denser 1×64 k-point mesh. The energy mesh cutoff for the real-space grid is chosen as 100 Hartree. We use 15 Å vacuum in the nonperiodic direction in order to remove the interaction between two periodic images.

III. RESULTS AND DISCUSSION

A. Atlas of spectral functions and spin textures in equilibrium

Monolayer TMDs exhibit a wide range of electronic properties—from semiconducting to semimetallic and metallic—depending on the electronic occupation of transition metal atoms and its coordination with the chalcogen atoms. The coordination can be either trigonal prismatic (1H) or octahedral phase (1T) [77], as illustrated in Fig. 1(d). For example, 1H-MoSe$_2$ and 1H-WSe$_2$ are semiconductors with a gap of $\simeq 2$ eV, whereas both the 1H and 1T phases of TaSe$_2$ are metallic [78]. The 1H phase has space group D_{3h}^1 (no. 187), which does not have the spatial inversion symmetry. On the other hand, 1T structure has space group of D_{3d}^1 (no. 164), which preserves the spatial inversion symmetry. Consequently, 1H phase of TMDs exhibits large SO splitting both in the conduction and valence bands [79], while SO coupling does not have any significant effect on the band structure of

1T phase [80]. However, in the bilayer geometry in Fig. 1, the structural inversion symmetry is broken at the interface even for 1T-TMD due to the presence of the Co layer.

The modification of spectral and spin textures within the Co layer due to SO coupling "injected" by monolayer TMD and/or structural inversion asymmetry are shown in Fig. 3. For comparison, reference spectral functions and spin textures on the surface of semi-infinite Co in contact with vacuum can be found in Figs. 4(a)–4(d) in Ref. [20]. Unlike those, where spin texture resembles the simple ones generated by the Rashba SO coupling in 2D electron gas with spin expectation values being tangent along the two Fermi circles, the spin textures in Fig. 3 are far more complex. Also, even though spectral functions on the Co side are similar when comparing Co/1H-MoSe$_2$ [Figs. 3(a)–3(f)] with Co/1H-WSe$_2$ [Figs. 3(g)–3(l)], or Co/1H-TaSe$_2$ [Figs. 3(m)–3(r)] with Co/1T-TaSe$_2$ [Figs. 3(s)–3(x)], the corresponding spin textures at the constant energy contours of spectral functions can be quite different. The appearance of spin textures on the fourth ML of Co demonstrates how SO coupling from TMD propagates into the bulk of FM and away from the interface.

B. Atlas of spin densities and SO torques out of equilibrium

When current flows through atomic planes with spin textures shown in Fig. 3, the imbalance between different $\mathbf{k}$ vectors is created which leads to nonzero nonequilibrium spin density $\mathbf{S}_{\text{CD}}(z)$ [Eq. (9)]. This is the manifestation of the so-called Edelstein effect [81,82], but for more complicated equilibrium spin textures in Fig. 3 instead of the simplistic ones of the Rashba type discussed in the original analysis [82]. Unlike the original analyses [81,82] or the recent Kubo formula calculations [69,86,88] of the Edelstein effect, which both require diffusive transport regime, our NEGF+ncDFT-based formalism applied to the Landauer setup in Fig. 1(c) makes possible also calculations in the ballistic transport regime [83,84]. The spatial profile of $\mathbf{S}_{\text{CD}}(z)$ within four different Co/TMD heterostructures in shown in Fig. 4 while orienting the magnetization of Co layer along three different axes. The integral of $\mathbf{S}_{\text{CD}} = \int dz \, \mathbf{S}_{\text{CD}}(z)$ within the volume of Co layer (composed of 2 MLs) gives total nonequilibrium spin density, and the orientation of its vector is visualized in Figs. 5(a)–5(c).

Due to assumed ballistic transport and absence of any spin Hall current along the z axis from the "bulk" of TMD layer, only $\mathbf{S}_{\text{CD}}^{\text{odd}} \neq 0$ is generated in Fig. 5. The generation of $\mathbf{S}_{\text{CD}}^{\text{even}} \neq 0$ is also possible [64] in the presence of skew scattering off impurities [85], where the impurity themselves can be spin independent [86,87] but spin textures (like the ones in Fig. 3) should contain an out-of-plane component [88]. In the analysis of SO torque, based on intuition from simplistic models like the 2D Rashba FM [52] or metallic surface of topological insulator covered by FM [53], one often assumes that $\mathbf{S}_{\text{CD}}^{\text{odd}} || \hat{y}$ for current flowing along the x axis, so that $\mathbf{T}_{\text{CD}}^{\text{odd}} \propto \hat{y} \times \mathbf{m}$. On the other hand, complexity of spin textures in Fig. 3 leads to $\mathbf{S}_{\text{CD}}^{\text{odd}}$ which changes direction as we reorient $\mathbf{m}_{\text{Co}}$. This leads to complex angular dependence of $\mathbf{T}_{\text{CD}}^{\text{odd}}$ component of SO torque, as is often observed experimentally [72] and in first-principles quantum transport calculations [16,40,64,87].

Inasmuch as the maximized value of $\mathbf{T}_{CD}^{odd}$ in Fig. 5(e) is found for Co/1H-WSe$_2$ heterostructure, we further investigate such complex angular dependence of $\mathbf{T}_{CD}^{odd}$ for this bilayer in Fig. 6. For this purpose, we rotate $\mathbf{m}_{Co}$ within three different planes and then fit the resulting SO torque curves using the following expansion [16,72]

$$\mathbf{T}_{CD}^{odd} = (\mathbf{p} \times \mathbf{m}_{Co}) \left[\sum_{n=0}^{\infty} T_{n\alpha} |\hat{z} \times \mathbf{m}_{Co}|^{2n} \right]$$

$$+ \mathbf{m}_{Co} \times (\hat{z} \times \mathbf{m}_{Co})(\mathbf{m}_{Co} \cdot \hat{x}) \left[\sum_{n=0}^{\infty} T_{n\beta} |\hat{z} \times \mathbf{m}_{Co}|^{2n} \right]. \tag{13}$$

The unit vector $\mathbf{p}$ can be determined by symmetry arguments [16] or calculated where we give its direction in Table I for both SO coupling in WSe$_2$ switched on ($\zeta_{WSe_2} \neq 0$) and off ($\zeta_{WSe_2} = 0$) in ncDFT calculations. The lowest order term $T_{0\alpha}(\mathbf{p} \times \mathbf{m}_{Co})$ in Eq. (13) is conventional FL torque [41,52], while higher order terms can have properties of both FL and DL torque [64]. The value of $T_{0\alpha}$, together with other non-negligible coefficients in Eq. (13), is given in Table I. Interestingly, even if $\zeta_{WSe_2} = 0$, so that interfacial SO coupling is possible only because of structural inversion asymmetry of the bilayer, these coefficients are nonzero in Table I. Upon switching the SO coupling on, $\zeta_{WSe_2} \neq 0$, the coefficients in Table I increase about five times when compared to those computed with $\zeta_{WSe_2} = 0$.

Finally, Fig. 7 demonstrates how SO proximity effect penetrating over an increasing number of Co MLs manifests in the physics of SO torque. That is, each ML of Co which acquires spin textures in Fig. 3 due to SO coupling "injected" by monolayer TMD will also generate nonequilibrium spin density $\mathbf{S}_{CD}(\mathbf{r})$ once the current flows through such ML. The noncollinearity between $\mathbf{S}_{CD}(\mathbf{r})$ and $\mathbf{B}_{XC}(\mathbf{r})$ within such ML then leads to nonzero local SO torque in Eq. (1). Figure 7 demonstrates that even 8th ML away from Co/1H-WSe$_2$ interface can exhibit SO torque, which means that SO proximity effect and thereby induced spin textures from Fig. 3 can propagate all the way to the opposite edge of thin layers of Co, at least in the clean limit.

IV. CONCLUSIONS

The recent experiments [89–94] on SO torque and spin-to-charge conversion [95] utilizing FM/TMD heterostructures have chosen a combination of these materials using usual "trial-and-error" procedure or generic symmetry arguments [91]. The application-geared arguments for the usage of such class of devices with monolayer TMDs are based on the fact that in traditional FM/heavy-metal SO torque devices [41], with many monolayers of heavy metal, spin Hall torque is

interfacial in nature and the bulk of heavy metal is of little use but it carries charge current and causes heat dissipation. Furthermore, the ratio between FL and DL components of SO torque, or spin-relaxation rate in spin-to-charge conversion experiments, can be effectively controlled via electric field by applying the back-gate voltage [93] to FM/TMD bilayers.

In this study, we demonstrate how to employ ncDFT calculations in order to obtain accurate Hamiltonian of FM/TMD interface in the representation of localized pseudoatomic orbitals. Such first-principles Hamiltonian is then combined with equilibrium GFs of nonperiodic heterostructures to compute spectral functions and spin textures at an arbitrary plane. In addition, first-principles GFs can be employed in quantum transport calculations to obtain nonequilibrium spin density and thereby driven SO torque. This makes it possible to precisely determine the most optimal materials combination for SO torque applications, where we find maximized SO torque in Co/WSe$_2$ bilayers among Co/1H-MoSe$_2$, Co/1H-WSe$_2$, Co/1H-TaSe$_2$, and Co/1T-TaSe$_2$ screened.

We note that SO proximity effect in a single ML of conventional 3d transition-metal ferromagnets Fe, Co, Ni due to adjacent TMD [96], topological insulator [97], or heavy metal (such as Pt [30]) layers has been studied recently with the focus on its impact on experimentally detectable [23] Gilbert damping enhancement [97] or introduction of Dzyaloshinskii-Moriya interaction giving rise to skyrmions [30,96]. In this study, we demonstrate that such SO proximity effect is not confined to just a single ML of conventional room temperature ferromagnetic metals, but it can propagate over many of their MLs. Furthermore, any ML near the interface with TMD which becomes SO proximitized, when brought out of equilibrium by passing current through it will generate nonequilibrium spin density as the key resource [29,41,43] for a variety of spintronic effects and applications.

Finally, we note that our calculations in the clean limit can be easily extended to take into account disorder effects due to impurities [16,64] or "frozen-phonons" and "frozen-magnons" [98]. These ingredients would be included in the Hamiltonian of larger supercells representing an ensemble of disorder configurations [99], so that $\mathbf{S}_{CD}$ and $\mathbf{T}_{CD}$ nonequilibrium quantities would then be averaged over such an ensemble. Unlike band structure of periodic lattices, spectral function remains well defined even in the presence of strong disorder blurring the original bands [99], so that analogous connections between spectral functions and textures and nonequilibrium spin densities could be explored, akin to what is conducted in this study.

[1] C. J. Kircher, Superconducting proximity effect of Nb, Phys. Rev. **168**, 437 (1968).

[2] J. J. Hauser, Magnetic proximity effect, Phys. Rev. **187**, 580 (1969).

[3] A. Altland, B. D. Simons, and D. T. Semchuk, Field theory of mesoscopic fluctuations insuperconductor-normal-metal systems, Adv. Phys. **49**, 321 (2000).

[4] S. Guéron, H. Pothier, N. O. Birge, D. Esteve, and M. H. Devoret, Superconducting Proximity Effect Probed on a Mesoscopic Length Scale, Phys. Rev. Lett. **77**, 3025 (1996).

[5] I. Žutić, A. Matos-Abiague, B. Scharf, H. Dery, and K. Belashchenko, Proximitized materials, Mater. Today **22**, 85 (2019).

[6] J. K. Freericks, B. K. Nikolić, and P. Miller, Tuning a Josephson junction through a quantum critical point, Phys. Rev. B **64**, 054511 (2001).

[7] J. K. Freericks, B. K. Nikolić, and P. Miller, Optimizing the speed of a Josephson junction with dynamical mean field theory, Int. J. Mod. Phys. B **16**, 531 (2002).

[8] B. K. Nikolić, J. K. Freericks, and P. Miller, Suppression of the "Quasiclassical" Proximity Gap in Correlated-Metal-Superconductor Structures, Phys. Rev. Lett. **88**, 077002 (2002).

[9] A. I. Buzdin, Proximity effects in superconductor-ferromagnet heterostructures, Rev. Mod. Phys. **77**, 935 (2005).

[10] K. Komatsu, C. Li, S. Autier-Laurent, H. Bouchiat, and S. Guéron, Superconducting proximity effect in long superconductor/graphene/superconductor junctions: From specular Andreev reflection at zero field to the quantum Hall regime, Phys. Rev. B **86**, 115412 (2012).

[11] Q. Li *et al.*, Proximity-induced superconductivity with subgap anomaly in type II Weyl semi-metal WTe$_2$, Nano Lett. **18**, 7962 (2018).

[12] M. A. Sillanpää, T. T. Heikkilä, R. K. Lindell, and P. J. Hakonen, Inverse proximity effect in superconductors near ferromagnetic material, Europhys. Lett. **56**, 590 (2001).

[13] W. L. Lim, N. Ebrahim-Zadeh, J. C. Owens, H. G. E. Hentschel, and S. Urazhdin, Temperature-dependent proximity magnetism in Pt, Appl. Phys. Lett. **102**, 162404 (2013).

[14] L. J. Zhu, D. C. Ralph, and R. A. Buhrman, Irrelevance of magnetic proximity effect to spin-orbit torques in heavy-metal/ferromagnet bilayers, Phys. Rev. B **98**, 134406 (2018)

[15] T. A. Peterson, A. P. McFadden, C. J. Palmstrøm, and P. A. Crowell, Influence of the magnetic proximity effect on spin-orbit torque efficiencies in ferromagnet/platinum bilayers, Phys. Rev. B **97**, 020403 (2018).

[16] K. D. Belashchenko, A. A. Kovalev, and M. van Schilfgaarde, First-principles calculation of spin-orbit torque in a Co/Pt bilayer, Phys. Rev. Materials **3**, 011401 (2019).

[17] K. Dolui and B. K. Nikolić, Spin-memory loss due to spin-orbit coupling at ferromagnet/heavy-metal interfaces: *Ab initio* spin-density matrix approach, Phys. Rev. B **96**, 220403(R) (2017).

[18] T. Shoman, A. Takayama, T. Sato, S. Souma, T. Takahashi, T. Oguchi, K. Segawa, and Y. Ando, Topological proximity effect in a topological insulator hybrid, Nat. Commun. **6**, 6547 (2015).

[19] C. D. Spataru and F. Léonard, Fermi-level pinning, charge transfer, and relaxation of spin-momentum locking at metal contacts to topological insulators, Phys. Rev. B **90**, 085115 (2014).

[20] J. M. Marmolejo-Tejada, P.-H. Chang, P. Lazić, S. Smidstrup, D. Stradi, K. Stokbro, and B. K. Nikolić, Proximity band structure and spin textures on both sides of topological-insulator/ferromagnetic-metal interface and their charge transport probes, Nano Lett. **17**, 5626 (2017).

[21] J. Zhang, J. P. Velev, X. Dang, and E. Y. Tsymbal, Band structure and spin texture of Bi$_2$Se$_3$/3d ferromagnetic metal interface, Phys. Rev. B **94**, 014435 (2016).

[22] Y.-T. Hsu, K. Park, and E.-A. Kim, Hybridization-induced interface states in a topological-insulator/ferromagnetic-metal heterostructure, Phys. Rev. B **96**, 235433 (2017).

[23] T. Liu *et al.*, Changes of Magnetism in a Magnetic Insulator Due to Proximity to a Topological Insulator, Phys. Rev. Lett. **125**, 017204 (2020).

[24] A. Bansil, H. Lin, and T. Das, *Colloquium:* Topological band theory, Rev. Mod. Phys. **88**, 021004 (2016).

[25] N. Nagaosa and Y. Tokura, Topological properties and dynamics of magnetic skyrmions, Nat. Nanotechnol. **8**, 899 (2013).

[26] O. Boulle *et al.*, Room-temperature chiral magnetic skyrmions in ultrathin magnetic nanostructures, Nat. Nanotechnol. **11**, 449 (2016).

[27] S. Woo *et al.*, Observation of room-temperature magnetic skyrmions and their current-driven dynamics in ultrathin metallic ferromagnets, Nat. Mater. **15**, 501 (2016).

[28] A. Soumyanarayanan *et al.*, Tunable room temperature magnetic skyrmions in Ir/Fe/Co/Pt multilayers, Nat. Mater. **16**, 898 (2017).

[29] A. Soumyanarayanan, N. Reyren, A. Fert, and C. Panagopoulos, Emergent phenomena induced by spin-orbit coupling at surfaces and interfaces, Nature (London) **539**, 509 (2016).

[30] E. Simon, L. Rózsa, K. Palotás, and L. Szunyogh, Magnetism of a Co monolayer on Pt(111) capped by overlayers of 5d elements: A spin-model study, Phys. Rev. B **97**, 134405 (2018).

[31] A. Tamai, W. Meevasana, P. D. C. King, C. W. Nicholson, A. de la Torre, E. Rozbicki, and F. Baumberger, Spin-orbit splitting of the Shockley surface state on Cu(111), Phys. Rev. B **87**, 075113 (2013).

[32] M. Gmitra, D. Kochan, P. Högl, and J. Fabian, Trivial and inverted Dirac bands and the emergence of quantum spin Hall states in graphene on transition-metal dichalcogenides, Phys. Rev. B **93**, 155104 (2016).

[33] K. Zollner and J. Fabian, Single and bilayer graphene on the topological insulator Bi$_2$Se$_3$: Electronic and spin-orbit properties from first principles, Phys. Rev. B **100**, 165141 (2019).

[34] T. Frank, M. Gmitra, and J. Fabian, Theory of electronic and spin-orbit proximity effects in graphene on Cu(111), Phys. Rev. B **93**, 155142 (2016).

[35] J. O. Island *et al.*, Spin-orbit-driven band inversion in bilayer graphene by the van der Waals proximity effect, Nature (London) **571**, 85 (2019).

[36] A. Dahal and M. Batzill, Graphene-nickel interfaces: A review, Nanoscale **6**, 2548 (2014).

[37] P. Lazić, K. D. Belashchenko, and I. Žutić, Effective gating and tunable magnetic proximity effects in two-dimensional heterostructures, Phys. Rev. B **93**, 241401 (2016).

[38] B. Scharf, G. Xu, A. Matos-Abiague, and I. Žutić, Magnetic Proximity Effects in Transition-Metal Dichalcogenides: Converting Excitons, Phys. Rev. Lett. **119**, 127403 (2017).

[39] A. Hallal, F. Ibrahim, H. Yang, S. Roche, and M. Chshiev, Tailoring magnetic insulator proximity effects in graphene: First-principles calculations, 2D Mater. **4**, 025074 (2017).

[40] K. Dolui, M. D. Petrović, K. Zollner, P. Plecháč, J. Fabian, and B. K. Nikolić, Proximity spin-orbit torque on a two-dimensional magnet within van der Waals heterostructure: Current-driven antiferromagnet-to-ferromagnet reversible

nonequilibrium phase transition in bilayer CrI_3, Nano Lett. **20**, 2288 (2020).

[41] A. Manchon, J. Železný, I. M. Miron, T. Jungwirth, J. Sinova, A. Thiaville, K. Garello, and P. Gambardella, Current-induced spin-orbit torques in ferromagnetic and antiferromagnetic systems, Rev. Mod. Phys. **91**, 035004 (2019).

[42] R. Ramaswamy, J. M. Lee, K. Cai, and H. Yang, Recent advances in spin-orbit torques: Moving towards device applications, Appl. Phys. Rev. **5**, 031107 (2018).

[43] W. Han, Y. Otani, and S. Maekawa, Quantum materials for spin and charge conversion, npj Quantum Mater. **3**, 27 (2018).

[44] Y. Tserkovnyak, A. Brataas, G. E. W. Bauer, and B. I. Halperin, Nonlocal magnetization dynamics in ferromagnetic heterostructures, Rev. Mod. Phys. **77**, 1375 (2005).

[45] S.-H. Chen, C.-R. Chang, J. Q. Xiao, and B. K. Nikolić, Spin and charge pumping in magnetic tunnel junctions with precessing magnetization: A nonequilibrium Green function approach, Phys. Rev. B **79**, 054424 (2009).

[46] F. Mahfouzi, J. Fabian, N. Nagaosa, and B. K. Nikolić, Charge pumping by magnetization dynamics in magnetic and semimagnetic tunnel junctions with interfacial rashba or bulk extrinsic spin-orbit coupling, Phys. Rev. B **85**, 054406 (2012).

[47] K. Dolui, U. Bajpai, and B. K. Nikolić, Spin-mixing conductance of ferromagnet/topological-insulator and ferromagnet/heavy-metal heterostructure: A first-principles Floquet-nonequilibrium Green function approach, arXiv:1905.01299.

[48] J. C. R. Sánchez, L. Vila, G. Desfonds, S. Gambarelli, J. P. Attané, J. M. D. Teresa, C. Magén, and A. Fert, Spin-to-charge conversion using Rashba coupling at the interface between non-magnetic materials, Nat. Commun. **4**, 2944 (2013).

[49] F. Mahfouzi, N. Nagaosa, and B. K. Nikolić, Spin-to-charge conversion in lateral and vertical topological-insulator/ferromagnet heterostructures with microwave-driven precessing magnetization, Phys. Rev. B **90**, 115432 (2014).

[50] K. Shen, G. Vignale, and R. Raimondi, Microscopic Theory of the Inverse Edelstein Effect, Phys. Rev. Lett. **112**, 096601 (2014).

[51] A. Manchon and S. Zhang, Theory of nonequilibrium intrinsic spin torque in a single nanomagnet, Phys. Rev. B **78**, 212405 (2008).

[52] K.-S. Lee, D. Go, A. Manchon, P. M. Haney, M. D. Stiles, H.-W. Lee, and K.-J. Lee, Angular dependence of spin-orbit spin-transfer torques, Phys. Rev. B **91**, 144401 (2015).

[53] P. B. Ndiaye, C. A. Akosa, M. H. Fischer, A. Vaezi, E.-A. Kim, and A. Manchon, Dirac spin-orbit torques and charge pumping at the surface of topological insulators, Phys. Rev. B **96**, 014408 (2017).

[54] K.-W. Kim, K.-J. Lee, J. Sinova, H.-W. Lee, and M. D. Stiles, Spin-orbit torques from interfacial spin-orbit coupling for various interfaces, Phys. Rev. B **96**, 104438 (2017).

[55] V. P. Amin, J. Zemen, and M. D. Stiles, Interface-Generated Spin Currents, Phys. Rev. Lett. **121**, 136805 (2018).

[56] S. Ghosh and A. Manchon, Spin-orbit torque in a three-dimensional topological insulator–ferromagnet heterostructure: Crossover between bulk and surface transport, Phys. Rev. B **97**, 134402 (2018).

[57] S. Haastrup *et al.*, The computational 2D materials database: high-throughput modeling and discovery of atomically thin crystals, 2D Mater. **5**, 042002 (2018).

[58] J. Zhou *et al.*, 2DMatPedia, an open computational database of two-dimensional materials from top-down and bottom-up approaches, Sci. Data **6**, 86 (2019).

[59] K. Andersen, S. Latini, and K. S. Thygesen, Dielectric genome of van der Waals heterostructures, Nano Lett. **15**, 4616 (2015).

[60] G. Stefanucci and R. van Leeuwen, *Nonequilibrium Many-Body Theory of Quantum Systems: A Modern Introduction* (Cambridge University Press, Cambridge, 2013).

[61] S. Wang, Y. Xu, and K. Xia, First-principles study of spin-transfer torques in layered systems with noncollinear magnetization, Phys. Rev. B **77**, 184430 (2008).

[62] M. O. A. Ellis, M. Stamenova, and S. Sanvito, Multiscale modeling of current-induced switching in magnetic tunnel junctions using ab initio spin-transfer torques, Phys. Rev. B **96**, 224410 (2017).

[63] B. K. Nikolić, K. Dolui, M. Petrović, P. Plecháč, T. Markussen, and K. Stokbro, First-principles quantum transport modeling of spin-transfer and spin-orbit torques in magnetic multilayers, in *Handbook of Materials Modeling: Applications: Current and Emerging Materials*, edited by W. Andreoni and S. Yip (Springer, Cham, 2018).

[64] K. D. Belashchenko, A. A. Kovalev, and M. van Schilfgaarde, Interfacial contributions to spin-orbit torque and magnetoresistance in ferromagnet/heavy-metal bilayers, Phys. Rev. B **101**, 020407 (2020).

[65] F. Mahfouzi and N. Kioussis, First-principles study of the angular dependence of the spin-orbit torque in Pt/Co and Pd/Co bilayers, Phys. Rev. B **97**, 224426 (2018).

[66] F. Mahfouzi, R. Mishra, P.-H. Chang, H. Yang, and N. Kioussis, Microscopic origin of spin-orbit torque in ferromagnetic heterostructures: A first-principles approach, Phys. Rev. B **101**, 060405 (2020).

[67] K. Capelle, G. Vignale, and B. L. Györffy, Spin Currents and Spin Dynamics in Time-Dependent Density-Functional Theory, Phys. Rev. Lett. **87**, 206403 (2001).

[68] F. G. Eich and E. K. U. Gross, Transverse Spin-Gradient Functional for Noncollinear Spin-Density-Functional Theory, Phys. Rev. Lett. **111**, 156401 (2013).

[69] F. Freimuth, S. Blügel, and Y. Mokrousov, Spin-orbit torques in Co/Pt(111) and Mn/W(001) magnetic bilayers from first principles, Phys. Rev. B **90**, 174423 (2014).

[70] F. Mahfouzi and B. K. Nikolić, How to construct the proper gauge-invariant density matrix in steady-state nonequilibrium: Applications to spin-transfer and spin-orbit torques, SPIN **3**, 1330002 (2013).

[71] W. M. Saslow, Landau-Lifshitz or Gilbert damping? That is the question, J. Appl. Phys. **105**, 07D315 (2009).

[72] K. Garello, I. M. Miron, C. O. Avci, F. Freimuth, Y. Mokrousov, S. Blügel, S. Auffret, O. Boulle, G. Gaudin, and P. Gambardella, Symmetry and magnitude of spin-orbit torques in ferromagnetic heterostructures, Nat. Nanotechnol. **8**, 587 (2013).

[73] F. Mahfouzi, B. K. Nikolić, and N. Kioussis, Antidamping spin-orbit torque driven by spin-flip reflection mechanism on the surface of a topological insulator: A time-dependent nonequilibrium Green function approach, Phys. Rev. B **93**, 115419 (2016).

[74] M. Schlipf and F. Gygi, Optimization algorithm for the generation of ONCV pseudopotentials, Comput. Phys. Commun. **196**, 36 (2015).

[75] S. Smidstrup *et al.*, QuantumATK: an integrated platform of electronic and atomic-scale modeling tools, J. Phys.: Condens. Matter **32**, 015901 (2019).

[76] J. P. Perdew, K. Burke, and M. Ernzerhof, Generalized Gradient Approximation Made Simple, Phys. Rev. Lett. **77**, 3865 (1996).

[77] C. Zhang *et al.*, Systematic study of electronic structure and band alignment of monolayer transition metal dichalcogenides in van der waals heterostructures, 2D Mater. **4**, 015026 (2016).

[78] M. D. Tran, J.-H. Kim, and Y. H. Lee, Tailoring photoluminescence of monolayer transition metal dichalcogenides, Curr. Appl. Phys. **16**, 1159 (2016).

[79] Z. Y. Zhu, Y. C. Cheng, and U. Schwingenschlögl, Giant spin-orbit-induced spin splitting in two-dimensional transition-metal dichalcogenide semiconductors, Phys. Rev. B **84**, 153402 (2011).

[80] J.-A. Yan, M. A. D. Cruz, B. Cook, and K. Varga, Structural, electronic and vibrational properties of few-layer 2H- and 1T-$TaSe_2$, Sci. Rep. **5**, 16646 (2015).

[81] A. G. Aronov and Y. B. Lyanda-Geller, Nuclear electric resonance and orientation of carrier spins by an electric field, JETP Lett. **50**, 431 (1989).

[82] V. M. Edelstein, Spin polarization of conduction electrons induced by electric current in two-dimensional asymmetric electron systems, Solid State Commun. **73**, 233 (1990).

[83] P.-H. Chang, T. Markussen, S. Smidstrup, K. Stokbro, and B. K. Nikolić, Nonequilibrium spin texture within a thin layer below the surface of current-carrying topological insulator Bi_2Se_3: A first-principles quantum transport study, Phys. Rev. B **92**, 201406(R) (2015).

[84] A. Kalitsov, S. A. Nikolaev, J. Velev, M. Chshiev, and O. Mryasov, Intrinsic spin-orbit torque in a single-domain nanomagnet, Phys. Rev. B **96**, 214430 (2017).

[85] D. A. Pesin and A. H. MacDonald, Quantum kinetic theory of current-induced torques in Rashba ferromagnets, Phys. Rev. B **86**, 014416 (2012).

[86] F. J. Sousa, G. Tatara, and A. Ferreira, Emergent spin-orbit torques in two-dimensional material/ferromagnet interfaces, arXiv:2005.09670.

[87] K. Zollner, M. D. Petrović, K. Dolui, P. Plecháč, B. K. Nikolić, and J. Fabian, Scattering-induced and highly tunable by gate damping-like spin-orbit torque in graphene doubly proximitized by two-dimensional magnet $Cr_2Ge_2Te_6$ and monolayer WS_2, Phys. Rev. Research **2**, 043057 (2020).

[88] M. Milletarì, M. Offidani, A. Ferreira, and R. Raimondi, Covariant Conservation Laws and the Spin Hall Effect in Dirac-Rashba Systems, Phys. Rev. Lett. **119**, 246801 (2017).

[89] J. Sklenar, W. Zhang, M. B. Jungfleisch, W. Jiang, H. Saglam, J. E. Pearson, J. B. Ketterson, and A. Hoffmann, Perspective: Interface generation of spin-orbit torques, J. Appl. Phys. **120**, 180901 (2016).

[90] Q. Shao, G. Yu, Y.-W. Lan, Y. Shi, M.-Y. Li, C. Zheng, X. Zhu, L.-J. Li, P. K. Amiri, and K. L. Wang, Strong Rashba-Edelstein effect-induced spinorbit torques in monolayer transition metal dichalcogenide/ferromagnet bilayers, Nano Lett. **16**, 7514 (2016).

[91] D. MacNeill, G. M. Stiehl, M. H. D. Guimaraes, R. A. Buhrman, J. Park, and D. C. Ralph, Control of spin-orbit torques through crystal symmetry in WTe_2/ferromagnet bilayers, Nat. Phys. **13**, 300 (2017).

[92] M. H. D. Guimarães, G. M. Stiehl, D. MacNeill, N. D. Reynolds, and D. C. Ralph, Spinorbit torques in $nbse_2$/permalloy bilayers, Nano Lett. **18**, 1311 (2018).

[93] W. Lv, Z. Jia, B. Wang, Y. Lu, X. Luo, B. Zhang, Z. Zeng, and Z. Liu, Electric-field control of spinorbit torques in WS_2/permalloy bilayers, ACS Appl. Mater. Interfaces **10**, 2843 (2018).

[94] S. Shi *et al.*, All-electric magnetization switching and Dzyaloshinskii-Moriya interaction in WTe_2/ferromagnet heterostructures, Nat. Nanotechnol. **14**, 945 (2019).

[95] C. Cheng *et al.*, Spin to charge conversion in MoS_2 monolayer with spin pumping, arXiv:1510.03451.

[96] S. Polesya, S. Mankovsky, D. Ködderitzsch, W. Bensch, and H. Ebert, Dzyaloshinskii-Moriya interactions and magnetic texture in Fe films deposited on transition-metal dichalcogenides, Phys. Status Solidi RRL **10**, 218 (2016).

[97] Y. Hou and R. Wu, Strongly Enhanced Gilbert Damping in 3d Transition-Metal Ferromagnet Monolayers in Contact with the Topological Insulator Bi_2Se_3, Phys. Rev. Applied **11**, 054032 (2019).

[98] A. A. Starikov, Y. Liu, Z. Yuan, and P. J. Kelly, Calculating the transport properties of magnetic materials from first principles including thermal and alloy disorder, noncollinearity, and spin-orbit coupling, Phys. Rev. B **97**, 214415 (2018).

[99] J. K. Glasbrenner, B. S. Pujari, and K. D. Belashchenko, Deviations from Matthiessen's rule and resistivity saturation effects in Gd and Fe from first principles, Phys. Rev. B **89**, 174408 (2014).